

Alcohol Assisted Solution-Combustion Technique for the Synthesis of Phase-Pure BaSnO₃ Nanoparticles at 130 °C

Sushobhita Chawla,[†] Garima Aggarwal,[†] Akash Kumar,^{†,‡} Akhilender Jeet Singh,[†]
and Balasubramaniam Kavaipatti*,[†]

[†]*Department of Energy Science and Engineering, IIT Bombay, Mumbai, India*

[‡]*Currently at: Department of Electronics Engineering, Gachon University, Republic of
Korea*

E-mail: bala.ramanathan@ese.iitb.ac.in

Abstract

Lowering the synthesis temperature to obtain phase pure BaSnO₃, which is the host material for high figure-of-merit (FOM) perovskite transparent conductors (TCs), can expand the horizons for its optoelectronic applications, with an obvious reduction in the thermal budget. In this work, we have developed a novel solution combustion technique for the synthesis of BaSnO₃ nanoparticles. A peroxy/superoxy precursor to the nanoparticles is first synthesized by co-precipitation of the tin and barium salts *via* the H₂O₂ assisted or the ‘CSMC’ route. The phase evolution, under different drying conditions of the wet precursor to crystalline BaSnO₃ nanoparticles is then studied. We find that the crystallization temperature of BaSnO₃ is significantly reduced by adding an organic solvent such as ethanol or propanol to the precursor; temperatures as low as 130 °C yield phase pure BaSnO₃ nanoparticles. We establish that the organic solvent increases the reactive O₂ ligand content, which plays a pivotal role in the synthesis.

Due to this, an exothermic reaction occurs around 130 °C, thereby providing the heat of reaction for conversion of the precursor to phase-pure BaSnO₃. Importantly, this method should also allow for the facile incorporation of dopants, paving the way for synthesis of high FOM TCs at low temperatures. Such low synthesis temperatures enable BaSnO₃ to be used in devices having temperature limitations during device processing, such as heterojunction Si solar cells or perovskite-based solar cells in an *n-i-p* architecture.

Introduction

Transparent conducting oxides (TCOs) offer contrasting properties of high transmittance in the visible region ($> 80\%$) with low resistivity ($< 10^{-3} \Omega\text{cm}$) and are continually being advanced for realization of high-performance optoelectronic devices. Among the available TCs, La-doped BaSnO₃, an n-type TCO ($E_g \sim 3.1 \text{ eV}$), has piqued scientific interest. This is due mainly to the discovery of an exceptional mobility in its bulk single-crystal¹ as well as MBE grown thin films.² An insulator in its stoichiometric form, the electrical properties of BaSnO₃ can be tuned by substitutional doping on Ba/Sn-site and/or oxygen vacancy doping.^{3–9} Owing to these properties BaSnO₃ has been utilized extensively as a gas/humidity sensor,^{10–13} photoanode in dye-sensitized solar cell (DSSC),^{14–17} protonic charge carrier in solid-oxide fuel cell (SOFC),¹⁸ electron transport layer in perovskite solar cell (PSC),^{19–21} and n-type channel in transistors.^{22,23} Although BaSnO₃ films can be obtained *via* both physical vapor deposition methods (MBE, PLD, sputtering *etc.*)^{2,10,11,24,25} and solution processing of nanoparticles,^{14–16,20,21} the former generally receives more attention for thin film applications. These methods are rigid as far as tuning of properties, scalability and compatibility with any underlying device components. Thermal degradation of the basal layers at high temperatures, interfacial diffusion deteriorating the electrical properties and thermodynamic instabilities at the interface are some of the problems encountered.^{26,27} An approach to circumvent these issues involves low-temperature solution processing of BaSnO₃ nanoparticles

synthesized *via* sol-gel, hydrothermal, co-precipitation or a variation of these. Further, these wet chemical techniques allow fine-tuning of the reaction conditions (temperature, concentration of reagents, additives or surfactants, pH, *etc.*) to achieve the desired properties. Hence, a more flexible and compatible low-temperature synthesis route based on a *chimie-douce* technique is necessitated for practical purposes.

Lowering the crystallization temperature of this material is an even more key issue in thin-film technologies. BaSnO₃ *via* wet chemical routes is synthesized over a range of temperatures, unto even 1000 °C.^{12,14,15,28–32} However, only a handful of reports on low-temperature ($T < 350$ °C) synthesis of BaSnO₃ exist.^{19,33,34} This further, is often accompanied by impurity phases.^{12,35–37} Only recently, Shin *et. al.* demonstrated a crystalline-superoxide molecular cluster (CSMC) route.¹⁹ This is based on the H₂O₂ assisted co-precipitation synthesis, to obtain BaSnO₃ nanoparticles at $T < 300$ °C. Then a precursor colloidal solution is developed begetting BaSnO₃ films at $T \sim 500$ °C.¹⁹ Following this, Shepherd *et. al.*³⁷ and Medvedev *et. al.*,³⁸ conducted a detailed study on this method to address the reproducibility issues and correctly identify the precursor, respectively. The various moieties present as ligands in the CSMC precursor are identified as a combination of hydroxo, hydroperoxo, peroxo, and superoxo species. These peroxide derivatives are known to decompose on exposure to moisture and/or temperature,^{39,40} which prompted us to explore the same.

In this work, we first study the degradation of the CSMC precursor on drying, a key issue previously not addressed. We find that synthesis of BaSnO₃ *via* this route is highly sensitive and inconsistent across the subjected drying conditions. However, we were able to identify an annealing protocol that enabled a reduction in synthesis temperature by 35%, giving T_{anneal} as low as 130 °C. The lowering of the crystallization temperature is an effect of adiabatic annealing conditions. More importantly, we establish that by the addition of an organic solvent such as ethanol, we can tune the nanoparticle size and phase purity. Drying of the precursors leads to a decrement in the superoxo/peroxo moiety. This is evinced by a change in color and different phase evolution routes taken by the various dried precursors. We find

that the addition of ethanol reverses this process and enables combustion in conjunction with the oxidizing precursors giving a new synthesis route akin to solution combustion synthesis. We further discuss the crucial parameters and features characteristic of this novel synthesis technique. A systematic analysis of the precursor stability and reactivity presented in this paper addresses the reasons for attaining phase pure BaSnO_3 at 130 °C. To the best of our knowledge, this is the lowest reported temperature for the synthesis of BaSnO_3 nanoparticles. The process developed in this study can be used as a template for low-temperature synthesis of other related compounds and improve their applicability in practical devices having the constraints of low-temperature fabrication steps.

Materials, methods and nomenclature

Materials

All chemicals were handled in air and used as-received, without further purification. Barium chloride dihydrate ($\text{BaCl}_2 \cdot 2\text{H}_2\text{O}$, purity $\geq 99\%$), tin (IV) chloride pentahydrate ($\text{SnCl}_4 \cdot 5\text{H}_2\text{O}$, purity $\geq 98\%$), and citric acid ($\text{C}_6\text{H}_8\text{O}_7$, purity $\geq 99.5\%$)

were purchased from Sigma-Aldrich. Reagent grade hydrogen peroxide (H_2O_2 , 30%), ammonium hydroxide (NH_4OH , 28%) were purchased from Honeywell Fluka and ethanol was purchased from Merck. Milli-Q (18.2 M Ω cm) deionized (DI) water was used in all synthesis and workup procedures.

Synthesis of BaSnO_3 Nanoparticles

The solution combustion synthesis of BaSnO_3 nanoparticles first follows the CSMC route employing $\text{BaCl}_2 \cdot 2\text{H}_2\text{O}$ and $\text{SnCl}_4 \cdot 5\text{H}_2\text{O}$ as the barium and tin source respectively.¹⁹ Fig 1 summarizes the process flow for the synthesis of BaSnO_3 nanoparticles. Equimolar amount of the precursors (10 mmol), along with citric acid as a chelating agent are added to 170 ml of H_2O_2 at 65 °C with continuous Ar purging. The pH of the reaction mixture is adjusted

to be in the range of 10 - 11 by adding 20 ml of ammonia solution, to surpass the solubility limit, allowing the intermediate to precipitate. After 2 hours, the products of reaction are washed thoroughly with DI water and ethanol, followed by centrifugation and decantation. Light yellow precipitates are obtained in this procedure. These precipitated precursors are then subjected to three different overnight drying conditions. The precipitates are either ambient dried (A), dried in a vacuum desiccator at room temperature (D), or dried in a hot air oven at 100 °C (O). The as-prepared or the undried precipitates (N) are separated from the supernatant by use of a filter paper, for analysis, before annealing. The precursors (~300 mg) are then mixed with 2 ml of ethanol and heated in a tube furnace at temperatures in the range of 110 ± 5 °C to 190 ± 5 °C for 30 minutes.

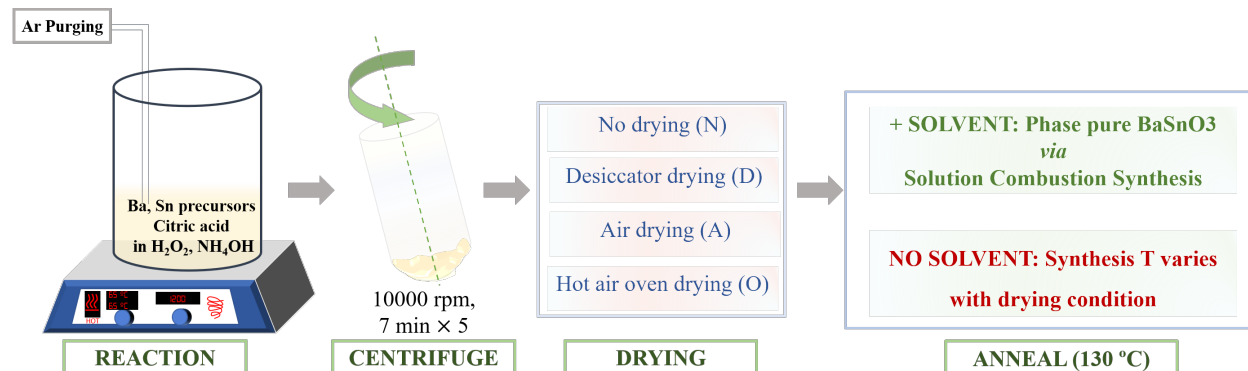


Figure 1: Process flow diagram for the synthesis of BaSnO₃ nanoparticles *via* solution combustion route.

Characterization

The crystalline structure was examined using an X-ray diffractometer (XRD, Rigaku Smart Lab) with a Cu K α radiation source operating at a voltage of 40 kV and 30 mA. Measurements were taken for 2θ values in the range 20 to 80° at a scan rate of 6 °/min. Fourier transform infrared (FTIR) spectra was obtained using 3000 Hyperion Microscope with Vertex 80 FTIR System Bruker, in KBr pressed discs. The spectra were taken in a transmission mode, over the range 390 to 3900 cm⁻¹. Changes in the precursor mass and the nature of

the reaction as a function of temperature were determined using thermogravimetric analysis (TGA/DT, NETZSCH-STA 449 F1, Jupiter) in a nitrogen atmosphere. High resolution transmission electron microscopy (Tecnai G2 F30, Fei, 300 kV) equipped with selected area electron diffractometry (SAED) was used to determine the microstructure and crystallinity of the synthesized nanoparticles. The simulated SAED patterns were produced using the Diffraction Ring Profiler software for phase confirmation of the synthesized nanoparticles.⁴¹

For the ease of identification the samples are labeled as "X_T_Et" where 'X' identifies the dried precursor state (N, A, D, or O), 'T' stands for the annealing temperature in degree Celsius (190 °C, 170 °C, 150 °C, 130 °C or 110 °C), and 'Et' for additional ethanol added to the precursor prior to the annealing. For example, precursors dried in hot air oven and then annealed at 150 °C without ethanol and with ethanol are termed "O_150" and "O_150_Et" respectively.

Results and discussion

Effect of drying conditions and identification of the reaction type

We investigated the effects of various drying conditions (ambient dry (A), desiccator dry (D), and oven-dry (O)) on the freshly centrifuged precipitates. This subsequently enabled gaining insights into the stability of the synthesized precursors against the subjected conditions. The immediate observation on drying was: the D precursors retained the yellow color observed in the as-centrifuged precipitates, however, the A and O precursors turned white, indicating some change in the precursor composition. Structural characterization (XRD) of the undried (N) and dried precursors (D, A, and O) is shown in Fig 2 (from top to bottom). At the bottom, XRD spectra of phase pure BaSnO₃ is provided and demarcated as gray dotted lines for the comparison [JCPDS: 00-015-0780]. The peaks observed in the XRD do not match with any phase constituted of the precursor elements but are left shifted compared to the standard XRD pattern of BaSnO₃. This shift is found to increase with the 2θ value,

indicating a uniformly expanded lattice of the precursors compared to phase pure BaSnO_3 . The crystalline phase constituting the precursor remains the same as depicted by consistent peak positions across all drying conditions and the as-prepared precipitates. A slight right shift in the case of oven-dried samples might be due to the drying temperature being 100°C and is attributed to a loss of water. This is expected, as on annealing a loss in water and other byproducts will eventually lead to phase pure BaSnO_3 .³⁴ The oven-drying temperature is although not enough to obtain phase pure BaSnO_3 . Further, the peak intensity (crystallinity) reduces with drying in the order: $\text{N} > \text{D} > \text{A} > \text{O}$. A decrement in crystallinity signifies an increase in some amorphous entity or decrease in long-range order in the crystalline precursor on drying. Since the crystallinity of precursors is not very good and, the XRD characterization of a material is limited appertaining to an amorphous entity, we analysed the samples *via* FTIR to probe further into this observation.

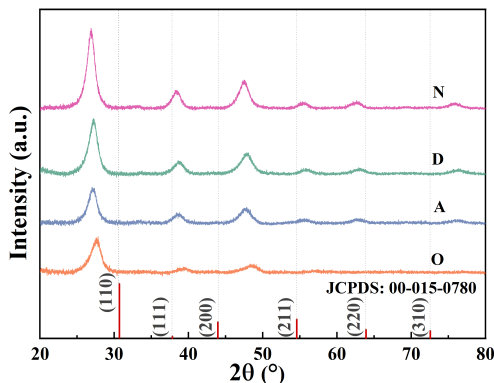


Figure 2: XRD patterns of the undried (N), ambient dried (A), desiccator dried (D), oven-dried (O) precursors and standard BaSnO_3 powder diffraction (from top to bottom). All XRD peaks of the four precursors coincide but have different peak intensities.

FTIR spectra of the three dried precursors, (a) D, (b) A, and (c) O is shown in Fig 3, from top to bottom. The method used to obtain FTIR uses dry powder samples mixed with KBr and pressed into pellets, which did not allow us to obtain the spectra of the undried precursors. In the figure the solid lines correspond to the FTIR recorded at room temperature and the dashed lines correspond to the FTIR of in-situ heated precursors at 150°C . Table 1 summarizes the vibrational peaks assigned to the various modes. The peak positions in

the three precursors at RT, as well as 150 °C are similar, however, the relative intensities corresponding to various vibrational bands vary. The spectrum confirms the presence of three different phases, one corresponding to the lattice water that has not been completely removed on drying or is due to absorption of moisture from the air, a carbonate phase evinced from the presence of carbonate vibrational peaks and the precursor phase consisting of a barium and tin peroxo/superoxo complex. The vertical lines represent the Sn-O (~ 520 and ~ 720 cm^{-1}) and Ba-O (~ 1420 cm^{-1}) vibrations. A broad band centered at 3400 cm^{-1} is attributed to the symmetric and antisymmetric -OH stretching from lattice water, the small peak at ~ 1630 cm^{-1} is due to the H-OH bending, while a shoulder peak at 1560 cm^{-1} is due to surface adsorbed water.⁴²⁻⁴⁴ The presence of just these three fundamental modes indicates that there is no coordinated water in the precursors. The absorption corresponding to carbonates appears at 850-860 cm^{-1} and 1420-1440 cm^{-1} , however, the latter one coincides with the asymmetric stretching mode of Ba-O. Nonetheless, simultaneous presence of the two carbonate absorption peaks confirm its presence and further is a common occurrence in barium compounds.^{36,45-48} The carbonate specie is suspected to be present as an amorphous phase and contributes to the background intensity in the XRD patterns. The spectra for all three precursors has similar peaks, with Ba-O and C-O peaks intensified in the case of O (denoted with a diamond, \blacklozenge , in the figure). The in-situ annealing results in all three spectra converging to the O spectra with an obvious reduction in the peaks corresponding to water. However, it does not lead to a BaSnO_3 pure phase as the peaks corresponding to Sn-O at ~ 725 and ~ 520 cm^{-1} , signifying more than one bonding pattern around the Sn atom, do not converge to the single characteristic vibrational mode of Sn-O which is typically observed at ~ 630 cm^{-1} .

Apparently, a temperature higher than 150 °C is required to obtain BaSnO_3 . As our ultimate goal is to get BaSnO_3 , we annealed these dried precursors around the literature reported value of 190 ± 5 °C. Since XRD and FTIR depict no significant difference between the various precursors, it is expected that all of them will convert to phase pure BaSnO_3 on

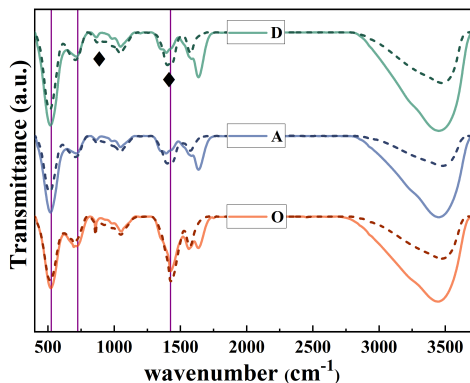


Figure 3: Infrared spectra of the precursors: D, A, and O (top to bottom), in KBr pellet obtained at RT (solid line, —) and 150 °C (dashed line, ---). The vertical lines represent the Sn-O (~ 520 and ~ 720 cm^{-1}) and Ba-O (~ 1420 cm^{-1}) vibrations. The C-O vibrational peaks are denoted by a diamond symbol(◆).

annealing. Fig 4 shows the XRD patterns for the four annealed powders N_190, A_190, D_190, and O_190. The immediate features of the analysis are: the precursors N & D that were yellow in color, convert to a BaSnO_3 phase, whereas the less crystalline white A & O precursors convert to an amorphous phase at this temperature. Although there is no significant difference in precursors' XRD & FTIR spectra, the phases that evolve on annealing are discordant. While some studies on the $\text{Ti-H}_2\text{O}_2$ catalytic system elucidate the connection of oxygen adducts and drying, colour change, reactivity, & rehydration, there is no such literature on Sn or its compounds.^{40,54,55} This study highlights such effects of drying on phase evolution of BaSnO_3 .

The nanoparticle size and/or crystallinity of the N_190 BaSnO_3 that had residual ethanol and water from the centrifuging step is distinctly different from the others. FTIR spectra of the dried precursors showed that the drying method is not successful in eliminating water hence, the presence of water is not something that could be affecting the morphology on annealing. It was then hypothesized that the oxidizing nature of the peroxo/superoxo precursor might be responsible for a reaction with ethanol to give a combustion reaction. This set our goal for the next course of study: (i) to mix the dried precursors with ethanol and anneal, to see if the dried precursors mixed with ethanol behave similar to N, (ii) verify if this is indeed a combustion reaction, and (iii) find the lowest temperature of synthesis

Table 1: FTIR frequency assignment for the precursors and synthesized nanoparticles

Wavenumber(cm^{-1})	Assignment	Reference
3600-3200	ν_s and ν_{as} (OH) stretching	43
1640	$\delta(\text{H}_2\text{O})$ scissoring	43
1560-1570	$\delta(\text{H}_2\text{O})$ scissoring, shoulder peak due to adsorbed water	44
1420-1440	ν_s and ν_{as} (Ba-O) stretching, ν (C-O) stretching in CO_3^{2-}	37,38
1380-1500	$\delta(\text{O-O-H})$ scissoring	19,38,49
1050	$\delta(\text{Sn-OH})$ scissoring	37,38,50
975	$\delta_s(\text{Sn-O-H})$	38,49
865	$\nu(\text{O-O})$ stretching	38,49
850-860	$\delta(\text{C-O})$ in CO_3^{2-} out of plane bending	37
725, 520	$\nu(\text{Sn-O-Sn})$ and $\nu(\text{Sn-O})$ from SnO_3^{2-}	37,38
630	$\nu_s(\text{Sn-O-Sn})$ stretching	51-53

achievable by this novel technique to synthesize phase pure BaSnO_3 nanoparticles.

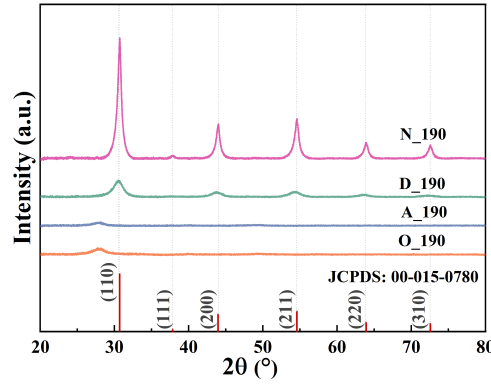


Figure 4: XRD patterns of all the precursors heat-treated at 190 °C without the addition of any ethanol (N_190, D_190, A_190, O_190, and standard BaSnO_3 powder diffraction, from top to bottom).

Towards this, we first mixed all the four precursors with ethanol, the color turned yellow instantly from white, qualitatively indicating a reversal of the peroxo/superoxo decomposition. We then annealed them at a temperature of 190 °C. The XRDs of the four annealed precipitates incontestably depict a highly crystalline BaSnO_3 phase (Fig 5). It is observed that ethanol facilitates the synthesis of BaSnO_3 at 190 °C irrespective of the drying condi-

tions, which otherwise plays a crucial role in the phase purity of the final product as shown in Fig 4. Although, N and D convert to BaSnO_3 irrespective of ethanol, the crystallinity and the nanoparticle size in the two methods differ substantially. The evident effect of ethanol addition prior to annealing reveals a new technique of synthesizing BaSnO_3 that progresses by a reaction between the peroxo/superoxo precursor and ethanol.

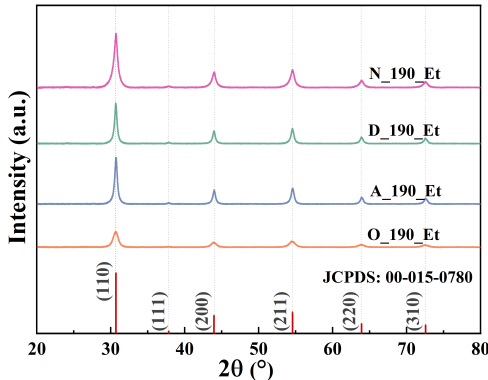


Figure 5: XRD patterns of all the ethanol mixed precursors heat treated at 190 °C (N_190_Et, D_190_Et, A_190_Et, O_190_Et, and standard BaSnO_3 powder diffraction, from top to bottom).

Further, the course of product formation taken by the two routes (ethanol devoid and ethanol assisted synthesis) also differed physically: the one with ethanol disintegrates with a ballistic reaction taking place within minutes to give fine BaSnO_3 nanoparticles. The reaction is believed to be a solution combustion synthesis wherein, annealing of a strong oxidising agent and fuel mixture in an appropriate solvent results in a highly exothermic reaction, enabling precursor conversion to BaSnO_3 at low temperatures.⁵⁶⁻⁶⁰ The oxidizing nature of the precursor phase is attributed to the low strength of the O-O in all peroxo compounds due to which they exhibit powerful oxidizing properties.³⁹ The addition of ethanol results in a combustion reaction in the solution phase, making this a solution combustion synthesis. We presumed a scope of further reduction in the synthesis temperature through this route due to the nature of the reaction that is observed.

Annealing temperature and characterization of the nanoparticles

As prepared undried precursors (N) were mixed with ethanol and annealed at temperatures ranging from 170 °C to 110 °C as shown in Fig 6. A pure BaSnO₃ phase is observed at temperatures all the way down to 130 °C. The crystallinity also remains independent of the annealing temperature until 130 °C. However, on a further reduction in temperature BaSnO₃ phase vanishes altogether and something akin to the precursor phase is seen. Hence, the lowest temperature that results in a pure BaSnO₃ phase is 130 °C. Even though this reduction in temperature from the previously reported value of 200 °C seems to be not so significant from thermal budget point of view, this will allow for integration of BaSnO₃, for instance, in perovskite solar cell device synthesis.

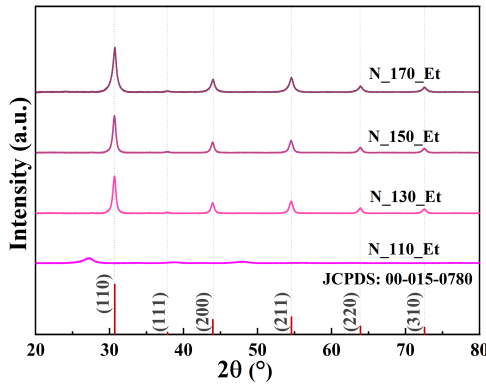


Figure 6: XRD of the undried precipitates (N) annealed with excess ethanol at temperatures 170 °C, 150 °C, 130 °C, 110 °C and standard BaSnO₃ powder diffraction (from top to bottom).

We also compared the N & D precursors annealed at this temperature by means of the two routes, *via* XRD and FTIR, shown in Fig 7 (a) and Fig 7 (b) respectively. Clearly, the desiccator dried precursors also gave a BaSnO₃ phase at this lowered temperature of 130 °C. This is lower than the literature reported values, which is believed to be due to annealing in a closed furnace providing adiabatic conditions as compared to annealing in open. It was also confirmed by heating the precursors on a hotplate where the minimum temperature of BaSnO₃ phase formation was approximately 200 °C. Further, it is seen that the ethanol assisted annealing gives very high crystallinity and a larger particle size compared to the

ethanol devoid ones. In the FTIR, existence of a carbonate phase is established by the band at $\sim 865\text{ cm}^{-1}$, which is absent in the ethanol assisted D_130_Et powders. Hence, desiccator drying followed by ethanol assisted annealing at $130\text{ }^{\circ}\text{C}$ leads to a highly crystalline phase pure BaSnO_3 with no carbonate byproducts. Adsorbed water also reduces drastically as evinced in the reduced intensity of the broad spectrum from $3000\text{--}3600\text{ cm}^{-1}$ in comparison to all other final products. Due to the combustion in presence of ethanol the local temperature is higher than the supplied temperature leading to a non-existent content of the thermally stable barium carbonate impurities, giving an increased yield and crystallite size of the perovskite BaSnO_3 phase.

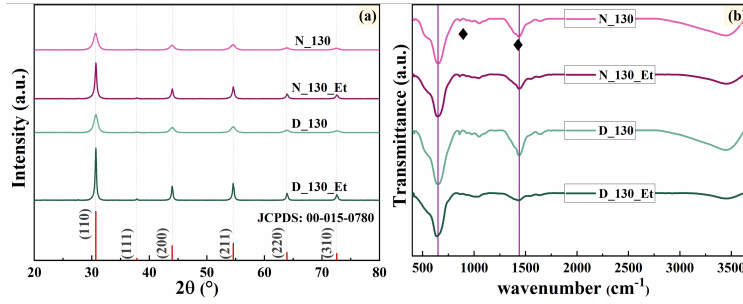


Figure 7: (a) XRD and (b) FTIR of the ethanol devoid and ethanol assisted BaSnO_3 nanoparticles synthesized from the undried (N) and desiccator dried (D) precursors at $130\text{ }^{\circ}\text{C}$ (N_130, N_130_Et, D_130, D_130_Et, and standard BaSnO_3 powder diffraction, from top to bottom).

To confirm the course and nature of the reaction thermal decomposition of the ethanol mixed D was examined by simultaneous differential thermal and thermogravimetry analysis (DTA/TGA) over a temperature range of RT to $600\text{ }^{\circ}\text{C}$ at a heating rate of $10\text{ }^{\circ}\text{C}/\text{min}$. Fig 8 shows the corresponding TGA-DT curves. The conversion of the precursor to phase pure BaSnO_3 is essentially a one-step process. There is some dehydration up to $130\text{ }^{\circ}\text{C}$ followed by an exothermic reaction at this temperature, where most of the mass is lost and pure BaSnO_3 remains. There is no significant weight loss or gain after this upto a temperature of $600\text{ }^{\circ}\text{C}$ signifying the reaction is essentially complete at $130\text{ }^{\circ}\text{C}$.

A nanostructural and morphological characterization was further performed by using TEM, high resolution TEM, and SAED techniques, confirming the polycrystalline nature of

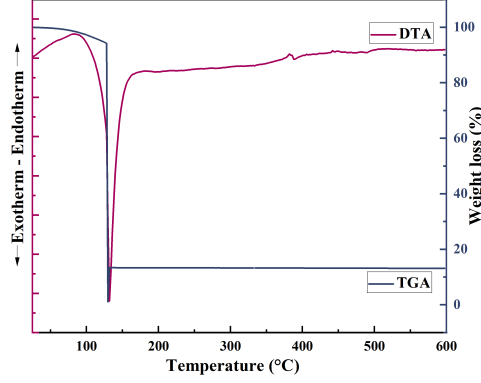


Figure 8: TGA-DTA curves of the desiccator dried (D) precipitates in nitrogen atmosphere from room temperature to 600 °C.

the nanoparticles formed *via* the two routes. The general morphology of the nanoparticles is shown in Fig 9 (a) and Fig 9 (d), with the difference in the nanoparticle size highlighted. High-resolution transmission electron microscopy (HRTEM) image of the nanoparticles is shown in Fig 9 (b) and Fig 9 (e). The lattice fringes clearly visible in the HRTEM image are indicative of crystallinity of the nanoparticles. The d-values obtained from HRTEM images are 2.86 Å and 2.08 Å for D_130 and 2.91 Å for D_130_Et, which are close to the theoretical d values corresponding to the (110) (d 2.91 Å) and (200) (d 2.058 Å) planes. The small dimensions of the nanoparticles do not allow the examination of a single nanoparticle by conventional selected area electron diffraction (SAED). Fig 9 (c) and Fig 9 (f) show the SAED pattern of the brightfield images of Fig 9 (a) and Fig 9 (d), respectively, and the corresponding simulation by diffraction ring profiler. A set of rings instead of spots due to the random orientation of the nanoparticles for both D_130 and D_130_Et is observed. The patterns index to the 110, 111, 200, 211, 220, 310, 222 and 321 reflexions of the cubic structure of BaSnO₃ [JCPDS: 00-015-0780]. This result is consistent with that of XRD and confirms that the as-synthesized BaSnO₃ nanoparticles are composed of pure cubic-phase.

The contrast in the XRD of the two routes can be attributed to a difference in the synthesized nanoparticles' size. This is further corroborated by carrying out a series of simulations of the XRD data by using the Crystal Maker® and Crystal Diffract® software packages. The simulation is initiated by using the available BaSnO₃ CIF file with lattice

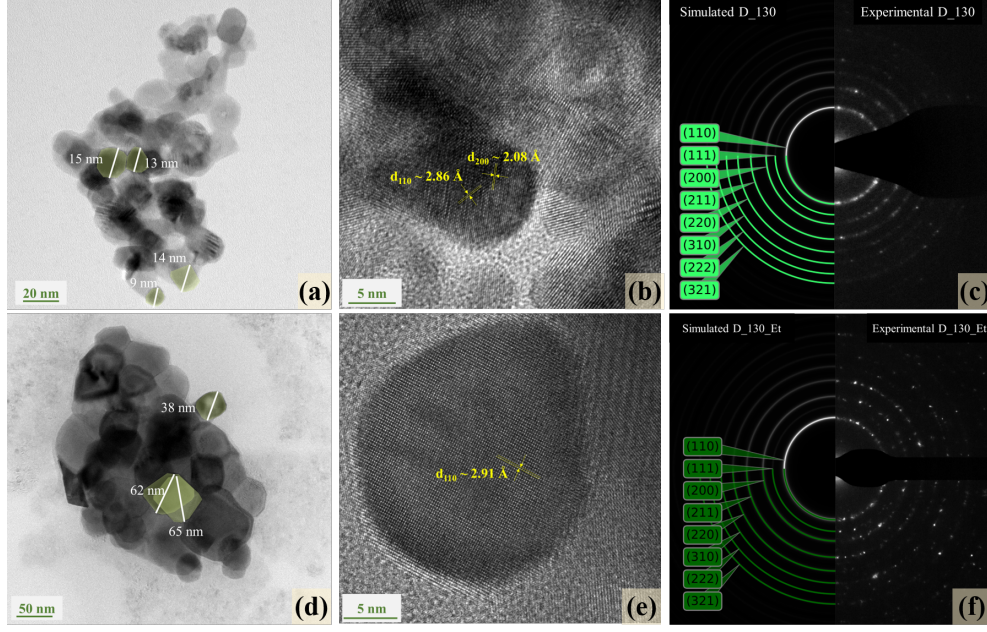


Figure 9: HRTEM images and SAED of the powders prepared at 130 °C without ethanol (a to c) and with ethanol (d to f).

parameter 4.11 Å and particle size calculated using the Scherrer equation, found to be 10 nm and 30 nm for D_130 and D_130_Et respectively. Fig 10 shows a fitting of 13 nm for D_130 nanoparticles and 36 nm for D_130_Et nanoparticles. Experimental and calculated XRD patterns are shown as solid and dotted lines, respectively. From the analysis, it is evident that there is an excellent agreement between the calculated and experimental fits for both the nanoparticles.

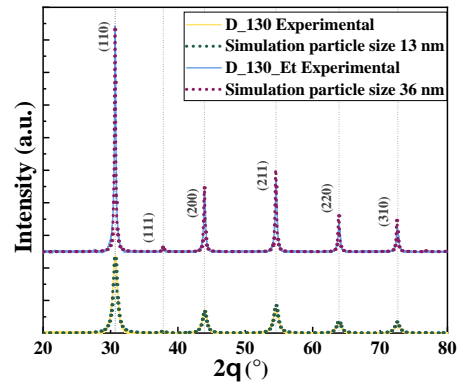


Figure 10: The experimental (solid line) and theoretical (dotted line) X-ray diffraction patterns for D_130 with particle size 12 nm and D_130_Et with particle size 36 nm.

The particle size difference for the two nanoparticles can be explained by the different synthesis route (combustion) taken by the precursor on annealing in presence of ethanol. In a typical combustion synthesis, the chemical energy released can rapidly heat the system to high temperatures $> 1800\text{ }^{\circ}\text{C}$, resulting in larger particle size. However, gaseous products released during combustion can disintegrate agglomerates and carry heat from the system, hindering further particle growth, giving uniformly distributed nanoparticles in terms of their size.⁶¹ The result is a truly polycrystalline nanopowder which is also clear by the SAED image. The role of ethanol is thus established as a fuel, in absence of which combustion does not take place. The ethanol devoid synthesis is also an exothermic reaction however, it is not combustion. Therefore the temperature of the system is roughly the supplied temperature and in ethanol assisted synthesis it reaches the flame temperatures. This results in uniformly distributed large particles when ethanol is used. In many a combustion synthesis citric acid also acts as a fuel,^{62–65} which in this reaction is employed as the chelating agent. To confirm the function of citric acid in the reaction, whether it enhances the combustion along with ethanol, we carried out the same procedure in absence of citric acid and is discussed in the following section.

Role of citric acid

In papers preceding this one, the role of citric acid has been established as a chelating agent, the one that limits and eventually prevents the crystallization of precursors to BaSnO_3 .³⁷ Hence, we did not work on optimizing the amount of citric acid needed, instead explored the necessity of citric acid in combustion synthesis at $130\text{ }^{\circ}\text{C}$. We, therefore, conducted the synthesis in the absence of citric acid, desiccator dried the precursors and annealed them. Fig 11 (a) shows the XRD of the desiccator dried precursors, the precursors annealed without ethanol and the precursors annealed with ethanol (bottom to top). The XRD confirms the phase conversion to BaSnO_3 .

To further comment on the morphology of the obtained nanoparticles, an FTIR and TEM

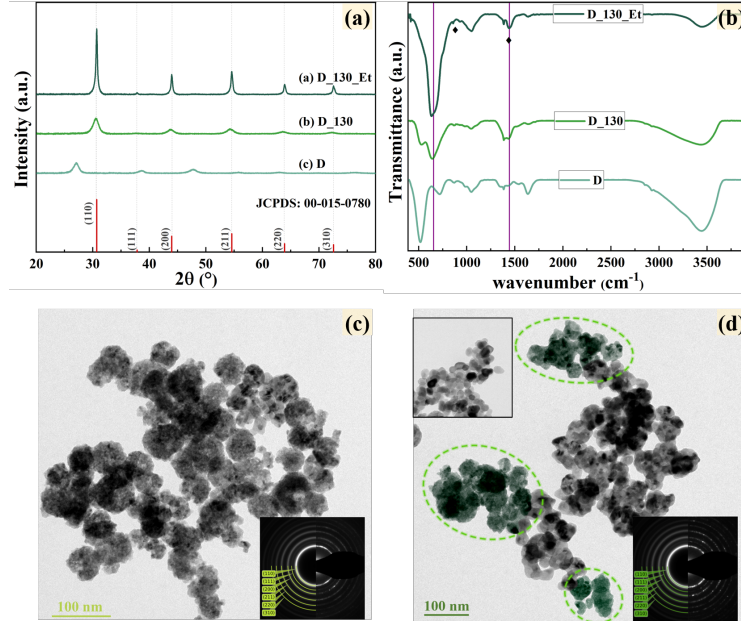


Figure 11: (a) XRD, and (b) FTIR of precursor synthesized without citric acid desiccator dried (D), D annealed at 130 °C, D mixed with ethanol and annealed at 130 °C, (c) TEM of the nanoparticles synthesized without citric acid and annealed at 130 °C, inset shows the corresponding experimental SAED pattern and simulated pattern using diffraction ring profiler (d) TEM of the nanoparticles synthesized without citric acid and annealed at 130 °C with ethanol, bottom inset shows the corresponding experimental SAED pattern and simulated pattern using diffraction ring profiler, inset at the top shows TEM image from a different region of the same nanoparticles.

analysis was done as shown in Fig 11 (b) and 11 (c) & 11(d)). The D (no citric acid) has its FTIR spectra similar to the one observed in citric acid assisted synthesis Fig 2. In the case of ethanol devoid synthesis, where XRD confirmed phase pure BaSnO_3 , FTIR shows clear signs of remnant precursor phase indicated by the presence of vibrational peaks at $\sim 520 \text{ cm}^{-1}$. At 130 °C in absence of ethanol, BaSnO_3 is obtained however it is accompanied by the unconverted precursor phase. The precursor does not uniformly convert to BaSnO_3 . Nanoparticles smaller than citric acid assisted counterpart agglomerated in a flowery pattern are observed and highlighted in the Fig 11 (c). In the case of ethanol assisted synthesis the effect of combustion is non-uniform, although phase purity is confirmed *via* XRD, FTIR and SAED, a mixed nanoparticle morphology is seen (Fig 11 (d)). The flowery morphology similar to the ethanol devoid synthesis is highlighted in the figure. Dispersed individual

nanoparticles similar to D_130_Et (Fig 9 (d)) are visible, however are scarce, an example image is shown in the inset of Fig 11 (d).

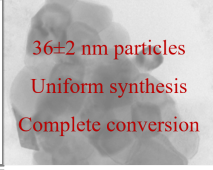
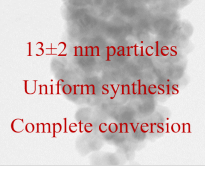
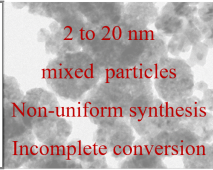
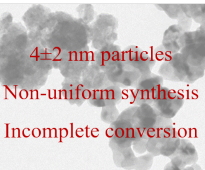
	Ethanol	No Ethanol
Citric Acid	 <p>36±2 nm particles Uniform synthesis Complete conversion</p>	 <p>13±2 nm particles Uniform synthesis Complete conversion</p>
No Citric Acid	 <p>2 to 20 nm mixed particles Non-uniform synthesis Incomplete conversion</p>	 <p>4±2 nm particles Non-uniform synthesis Incomplete conversion</p>

Figure 12: Summary of the interplay of ethanol and citric acid in combustion synthesis of BaSnO_3 at 130 °C.

The citric acid should be an aid in combustion and phase conversion at this low a temperature. It helps in the uniform distribution of the exothermic conversion energy over the precursor area when the precursor is annealed. On a first inspection, it seems that citric acid in the reaction plays no significant role. However, at low temperatures (130 °C) when the sole supply of phase converting heat energy is from exothermicity of reaction, citric acid being an organic compound becomes essential for phase purity. It thus plays a dual role of chelating agent and supporting combustion. We reckon that at higher synthesis temperatures employed in the previous reports the effect might either be counterbalanced due to thermal effects, or there has been no further analysis than XRD, which in our case proves to be limited. Fig 12 summarizes the combined effect of citric acid and ethanol on the synthesis of BaSnO_3 . This work construes the interplay of citric acid and ethanol in controlling nanoparticle size and phase purity. A further study into the different morphological development in thin films *via* this method may provide a basis to obtain unique properties, and will be explored in a subsequent study.

Conclusions

In this paper, we have undertaken a systematic study of BaSnO_3 synthesis *via* a novel combustion technique. In particular, the temperature and moisture effects of drying lead to a degradation of the superoxo/peroxo precursors, precluding low-temperature synthesis of BaSnO_3 . We propose and demonstrate that ethanol reconverts the unreactive dried precursors to reactive peroxo phase along with acting as a fuel in combustion. Our method which is an extension of the CSMC synthesis, guarantees low-temperature obtention of BaSnO_3 powder regardless of the drying condition. Phase pure BaSnO_3 is obtained at temperatures as low as 130 °C, which is the lowest temperature reported for such highly crystalline nanoparticles. The phase purity, particle size (35 ± 2 nm) and distribution characteristic of high-temperature synthesis attained at such a low temperature is attributed to a combustion synthesis. This combustion takes place in a single step, which is a highly exothermic process and results in a uniform morphology when both citric acid and ethanol are present. Foremost, this work provides a facile recipe for the synthesis of a technologically important material BaSnO_3 with morphology typical of high-temperature routes. This paves a way to obtain high quality nanoparticles, that attracts many device oriented applications such as carrier selective contacts, transparent conductors and channel material of a thin film transistor *etc.*, at low temperatures.

Acknowledgement

The authors acknowledge the financial support received by the National Centre for Photovoltaic Research and Education (NCPRE) through funding (16MNRE002) from the Ministry of New and Renewable Energy, Government of India. The authors thank Prof. Pratibha Sharma, DESE, IIT Bombay, for granting access to the TGA-DTA facilities. The authors also thank SAIF and IRCC at IIT Bombay for providing access to the characterization facilities.

References

- (1) Kim, H. J.; Kim, U.; Kim, T. H.; Mun, H. S.; Jeon, B.-G.; Hong, K. T.; Lee, W.-J.; Ju, C.; Kim, K. H.; Char, K. High mobility in a stable transparent perovskite oxide. *Appl. Phys. Express* **2012**, *5*, 061102.
- (2) Paik, H. et al. Adsorption-controlled growth of La-doped BaSnO₃ by molecular-beam epitaxy. *APL Mater.* **2017**, *5*, 116107.
- (3) Mizoguchi, H.; Chen, P.; Boolchand, P.; Ksenofontov, V.; Felser, C.; Barnes, P. W.; Woodward, P. M. Electrical and optical properties of Sb-doped BaSnO₃. *Chem. Mater.* **2013**, *25*, 3858–3866.
- (4) Lee, S.; Wang, H.; Gopal, P.; Shin, J.; Jaim, H. M. I.; Zhang, X.; Jeong, S. Y.; Usanmaz, D.; Curtarolo, S.; Fornari, M.; Buongiorno Nardelli, M.; Takeuchi, I. Systematic band gap tuning of BaSnO₃ via chemical substitutions: The role of clustering in mixed-valence perovskites. *Chem. Mater.* **2017**, *29*, 9378–9385.
- (5) Kumar, A.; Singh, B. P.; Choudhary, R. N. P.; Thakur, A. K. A.C. Impedance analysis of the effect of dopant concentration on electrical properties of calcium modified BaSnO₃. *J. Alloys Compd.* **2005**, *394*, 292–302.
- (6) Fan, F.-Y.; Zhao, W.-Y.; Chen, T.-W.; Yan, J.-M.; Ma, J.-P.; Guo, L.; Gao, G.-Y.; Wang, F.-F.; Zheng, R.-K. Excellent structural, optical, and electrical properties of Nd-doped BaSnO₃ transparent thin films. *Appl. Phys. Lett.* **2018**, *113*, 202102.
- (7) Jaim, H. M. I.; Lee, S.; Zhang, X.; Takeuchi, I. Stability of the oxygen vacancy induced conductivity in BaSnO₃ thin films on SrTiO₃. *Appl. Phys. Lett.* **2017**, *111*, 172102.
- (8) Luo, B.; Hu, J. Unraveling the oxygen effect on the properties of sputtered BaSnO₃ thin films. *ACS Appl. Electron. Mater.* **2019**, *1*, 51–57.

- (9) Cho, H. J.; Onozato, T.; Wei, M.; Sanchela, A.; Ohta, H. Effects of vacuum annealing on the electron mobility of epitaxial La-doped BaSnO₃ films. *APL Mater.* **2019**, *7*, 022507.
- (10) Ostrick, B.; Fleischer, M.; Lampe, U.; Meixner, H. Preparation of stoichiometric barium stannate thin films: Hall measurements and gas sensitivities. *Sens. Actuators, B* **1997**, *44*, 601–606.
- (11) Lampe, U.; Gerblinger, J.; Meixner, H. Nitrogen oxide sensors based on thin films of BaSnO₃. *Sens. Actuators, B* **1995**, *26*, 97–98.
- (12) Tao, S.; Gao, F.; Liu, X.; Sørensen, O. T. Ethanol-sensing characteristics of barium stannate prepared by chemical precipitation. *Sens. Actuators, B* **2000**, *71*, 223–227.
- (13) Viviani, M.; Buscaglia, M. T.; Buscaglia, V.; Leoni, M.; Nanni, P. Barium perovskites as humidity sensing materials. *J. Eur. Ceram. Soc.* **2001**, *21*, 1981–1984.
- (14) Shin, S. S.; Kim, J. S.; Suk, J. H.; Lee, K. D.; Kim, D. W.; Park, J. H.; Cho, I. S.; Hong, K. S.; Kim, J. Y. Improved quantum efficiency of highly efficient perovskite BaSnO₃-based dye-sensitized solar cells. *ACS Nano* **2013**, *7*, 1027–1035.
- (15) Kim, D. W.; Shin, S. S.; Lee, S.; Cho, I. S.; Kim, D. H.; Lee, C. W.; Jung, H. S.; Hong, K. S. BaSnO₃ perovskite nanoparticles for high efficiency dye-sensitized solar cells. *ChemSusChem* **2013**, *6*, 449–454.
- (16) Xie, F.; Li, Y.; Xiao, T.; Shen, D.; Wei, M. Efficiency improvement of dye-sensitized BaSnO₃ solar cell based surface treatments. *Electrochim. Acta* **2018**, *261*, 23–28.
- (17) Roy, A.; Das, P. P.; Selvaraj, P.; Sundaram, S.; Devi, P. S. Perforated BaSnO₃ nanorods exhibiting enhanced efficiency in dye sensitized solar cells. *ACS Sustainable Chem. Eng.* **2018**, *6*, 3299–3310.

- (18) Exner, J.; Nazarenus, T.; Kita, J.; Moos, R. Dense Y-doped ion conducting perovskite films of BaZrO₃, BaSnO₃, and BaCeO₃ for SOFC applications produced by powder aerosol deposition at room temperature. *Int. J. Hydrogen Energy* **2020**, *45*, 10000–10016.
- (19) Shin, S. S.; Yeom, E. J.; Yang, W. S.; Hur, S.; Kim, M. G.; Im, J.; Seo, J.; Noh, J. H.; Seok, S. I. Colloidally prepared La-doped BaSnO₃ electrodes for efficient, photostable perovskite solar cells. *Science* **2017**, *356*, 167–171.
- (20) Sun, C.; Guan, L.; Guo, Y.; Fang, B.; Yang, J.; Duan, H.; Chen, Y.; Li, H.; Liu, H. Ternary oxide BaSnO₃ nanoparticles as an efficient electron-transporting layer for planar perovskite solar cells. *J. Alloys Compd.* **2017**, *722*, 196–206.
- (21) Dileep K, R.; Rajbhar, M. K.; Ashina, A.; Ramasamy, E.; Mallick, S.; Rao, T. N.; Veerappan, G. A facile co-precipitation method for synthesis of Zn doped BaSnO₃ nanoparticles for photovoltaic application. *Mater. Chem. Phys.* **2021**, *258*, 123939.
- (22) Park, C.; Kim, U.; Ju, C. J.; Park, J. S.; Kim, Y. M.; Char, K. High mobility field effect transistor based on BaSnO₃ with Al₂O₃ gate oxide. *Appl. Phys. Lett.* **2014**, *105*, 203503.
- (23) Kim, Y. M.; Park, C.; Kim, U.; Ju, C.; Char, K. High-mobility BaSnO₃ thin-film transistor with HfO₂ gate insulator. *Appl. Phys. Express* **2015**, *9*, 011201.
- (24) Kumar, A.; Maurya, S.; Chawla, S.; Patwardhan, S.; Kavaipatti, B. Effect of thickness on metal to semiconductor transition in La doped BaSnO₃ films deposited on high mismatch LSAT substrates. *Appl. Phys. Lett.* **2019**, *114*, 212103.
- (25) Kumar, A.; Maurya, S.; Patwardhan, S.; Balasubramaniam, K. R. Opto-electronic properties of poly-crystalline La doped BaSnO₃ films deposited on quartz substrates. *J. Phys. D: Appl. Phys.* **2021**, *54*, 185108.

- (26) Zhang, Y.; Ng, S.-W.; Lu, X.; Zheng, Z. Solution-Processed Transparent Electrodes for Emerging Thin-Film Solar Cells. *Chem. Rev.* **2020**, *120*, 2049–2122.
- (27) Wang, Z.; Paik, H.; Chen, Z.; Muller, D. A.; Schlom, D. G. Epitaxial integration of high-mobility La-doped BaSnO₃ thin films with silicon. *APL Mater.* **2019**, *7*, 022520.
- (28) Pfaff, G. Wet chemical synthesis of BaSnO₃ and Ba₂SnO₄ powders. *J. Eur. Ceram. Soc.* **1993**, *12*, 159–164.
- (29) Bao, M.; Li, W.; Zhu, P. Study on the dielectric properties of oxide-doped Ba(Ti,Sn)O₃ ceramics prepared from ultrafine powder. *J. Mater. Sci.* **1993**, *28*, 6617–6621.
- (30) Leoni, M.; Viviani, M.; Nanni, P.; Buscaglia, V. Low-temperature aqueous synthesis (LTAS) of ceramic powders with perovskite structure. *J. Mater. Sci. Lett.* **1996**, *15*, 1302–1304.
- (31) Licheron, M.; Jouan, G.; Husson, E. Characterization of BaSnO₃ powder obtained by a modified sol-gel route. *J. Eur. Ceram. Soc.* **1997**, *17*, 1453–1457.
- (32) Liu, J.; Guan, Y.; Liu, S.; Li, S.; Gao, C.; Du, J.; Qiu, C.; Li, D.; Zhang, D.; Wang, X.; Wang, Y.; Hu, Y.; Rong, Y.; Mei, A.; Han, H. Modulating Oxygen Vacancies in BaSnO₃ for Printable Carbon-Based Mesoscopic Perovskite Solar Cells. *ACS Appl. Energy Mater.* **2021**, *Article ASAP*, (accessed 2021–10–21).
- (33) Kutty, T. R. N.; Vivekanadan, R. BaSnO₃ fine powders from hydrothermal preparations. *Mater. Res. Bull.* **1987**, *22*, 1457–1465.
- (34) Huang, C.; Wang, X.; Shi, Q.; Liu, X.; Zhang, Y.; Huang, F.; Zhang, T. A facile peroxo-precursor synthesis method and structure evolution of large specific surface area mesoporous BaSnO₃. *Inorg. Chem.* **2015**, *54*, 4002–4010.
- (35) Udawatte, C. P.; Kakihana, M.; Yoshimura, M. Preparation of pure perovskite-type

- BaSnO₃ powders by the polymerized complex method at reduced temperature. *Solid State Ion.* **1998**, *108*, 23–30.
- (36) Marikutsa, A.; Rumyantseva, M.; Baranchikov, A.; Gaskov, A. Nanocrystalline BaSnO₃ as an alternative gas sensor material: surface reactivity and high sensitivity to SO₂. *Materials* **2015**, *8*, 6437–6454.
- (37) Shepherd, W.; Wilms, M.; van Embden, J.; Gaspera, E. D. Accurate control of stoichiometry and doping in barium stannate perovskite oxide nanoparticles. *Chem. Commun.* **2019**, *55*, 11880–11883.
- (38) Medvedev, A. G.; Mikhaylov, A. A.; Shames, A. I.; Ilyukhin, A. B.; Churakov, A. V.; Grishanov, D. A.; Mel'nik, E. A.; Tripol'skaya, T. A.; Lev, O.; Prihodchenko, P. V. Identification of barium hydroxo-hydroperoxostannate precursor for low-temperature formation of perovskite barium stannate. *Inorg. Chem.* **2020**, *59*, 18358–18365.
- (39) Jakob, H.; Leininger, S.; Lehmann, T.; Jacobi, S.; Gutewort, S. Peroxo compounds, inorganic. *Ullmann's encyclopedia of industrial chemistry* **2007**, 293–324.
- (40) Bonino, F.; Damin, A.; Ricchiardi, G.; Ricci, M.; Spanò, G.; D'Aloisio, R.; Zecchina, A.; Lamberti, C.; Prestipino, C.; Bordiga, S. Ti-peroxo species in the TS-1/H₂O₂/H₂O system. *J. Phys. Chem. B* **2004**, *108*, 3573–3583.
- (41) Zhang, L.; Holt, C. M. B.; Luber, E. J.; Olsen, B. C.; Wang, H.; Danaie, M.; Cui, X.; Tan, X.; Lui, V. W.; Kalisvaart, W. P.; Mitlin, D. High rate electrochemical capacitors from three-dimensional arrays of vanadium nitride functionalized carbon nanotubes. *J. Phys. Chem. C* **2011**, *115*, 24381–24393.
- (42) Nakamoto, K. *Infrared and Raman spectra of inorganic and coordination compounds Part A*, 6th ed.; Wiley, 2006.

- (43) Nakamoto, K. *Infrared and Raman spectra of inorganic and coordination compounds Part B*, 6th ed.; Wiley, 2009.
- (44) Kevorkyants, R.; Rudakova, A. V.; Chizhov, Y. V.; Bulanin, K. M. The origin of 1560cm^{-1} band in experimental IR spectra of water adsorbed on TiO_2 surface: Ab initio assessment. *Chem. Phys. Lett.* **2016**, *662*, 97–101.
- (45) Mizoguchi, H.; Woodward, P. M.; Park, C.-H.; Keszler, D. A. Strong near-infrared luminescence in BaSnO_3 . *J. Am. Chem. Soc.* **2004**, *126*, 9796–9800.
- (46) Blanco-Lopez, M. C.; Rand, B.; Riley, F. L. The properties of aqueous phase suspensions of barium titanate. *J. Eur. Ceram. Soc.* **1997**, *17*, 281–287.
- (47) Cerdà, J.; Arbiol, J.; Diaz, R.; Dezanneau, G.; Morante, J. R. Synthesis of perovskite-type BaSnO_3 particles obtained by a new simple wet chemical route based on a sol–gel process. *Mater. Lett.* **2002**, *56*, 131–136.
- (48) López, M. D. B.; Fourlaris, G.; Rand, B.; Riley, F. L. Characterization of barium titanate powders: barium carbonate identification. *J. Am. Ceram. Soc.* **1999**, *82*, 1777–1786.
- (49) Sladkevich, S.; Gutkin, V.; Lev, O.; Legurova, E. A.; Khabibulin, D. F.; Fedotov, M. A.; Uvarov, V.; Tripol'skaya, T. A.; Prikhodchenko, P. V. Hydrogen peroxide induced formation of peroxystannate nanoparticles. *J. Sol-Gel Sci. Technol.* **2009**, *50*, 229–240.
- (50) Mizoguchi, H.; Bhuvanesh, N. S. P.; Kim, Y.-I.; Ohara, S.; Woodward, P. M. Hydrothermal crystal growth and structure determination of double hydroxides $\text{LiSb}(\text{OH})_6$, $\text{BaSn}(\text{OH})_6$, and $\text{SrSn}(\text{OH})_6$. *Inorg. Chem.* **2014**, *53*, 10570–10577.
- (51) Shan, C.; Huang, T.; Zhang, J.; Han, M.; Li, Y.; Hu, Z.; Chu, J. Optical and Electrical Properties of Sol–Gel Derived $\text{Ba}_{1-x}\text{La}_x\text{SnO}_3$ Transparent Conducting Films for Potential Optoelectronic Applications. *J. Phys. Chem. C* **2014**, *118*, 6994–7001.

- (52) Sarkar, A.; De, S. K. Defect and optical properties of Sb doped and hydrogenated BaSnO₃. *Semicond. Sci. Technol.* **2018**, *33*, 035018.
- (53) Deepa, A. S.; Vidya, S.; Manu, P. C.; Solomon, S.; John, A.; Thomas, J. K. Structural and optical characterization of BaSnO₃ nanopowder synthesized through a novel combustion technique. *J. Alloys Compd.* **2011**, *509*, 1830–1835.
- (54) Tengvall, P.; Bertilsson, L.; Liedberg, B.; Elwing, H.; Lundström, I. Degradation of dried Ti-peroxy gels made from metallic titanium and hydrogen peroxide. *J. Colloid Interface Sci.* **1990**, *139*, 575–580.
- (55) Francatto, P.; Souza Neto, F. N.; Nogueira, A. E.; Kubo, A. M.; Ribeiro, L. S.; Gonçalves, L. P.; Gorup, L. F.; Leite, E. R.; Camargo, E. R. Enhanced reactivity of peroxo-modified surface of titanium dioxide nanoparticles used to synthesize ultrafine bismuth titanate powders at lower temperatures. *Ceram. Int.* **2016**, *42*, 15767–15772.
- (56) Luo, X.-x.; Cao, W.-h. Ethanol-assistant solution combustion method to prepare La₂O₂S:Yb,Pr nanometer phosphor. *J. Alloys Compd.* **2008**, *460*, 529–534.
- (57) Kim, M.-G.; Kanatzidis, M. G.; Facchetti, A.; Marks, T. J. Low-temperature fabrication of high-performance metal oxide thin-film electronics via combustion processing - Nature Materials. *Nat. Mater.* **2011**, *10*, 382–388.
- (58) Varma, A.; Mukasyan, A. S.; Rogachev, A. S.; Manukyan, K. V. Solution combustion synthesis of nanoscale materials. *Chem. Rev.* **2016**, *116*, 14493–14586.
- (59) Maino, G.; Carleer, R.; Marchal, W.; Bonneux, G.; Hardy, A.; Van Bael, M. K. Remarkable lowering in the synthesis temperature of LiMn₂O₄ via citrate solution-gel synthesis facilitated by ethanol. *Dalton Trans.* **2017**, *46*, 14934–14946.
- (60) Novitskaya, E.; Kelly, J. P.; Bhaduri, S.; Graeve, O. A. A review of solution combustion

- synthesis: an analysis of parameters controlling powder characteristics. *Int. Mater. Rev.* **2021**, *66*, 188–214.
- (61) Shea, L. E.; McKittrick, J.; Lopez, O. A.; Sluzky, E.; Phillips, M. L. F. Advantages of self-propagating combustion reactions for synthesis of oxide phosphors. *J. Soc. Inf. Disp.* **1997**, *5*, 117–125.
- (62) Deshpande, K.; Mukasyan, A.; Varma, A. Direct Synthesis of Iron Oxide Nanopowders by the Combustion Approach: Reaction Mechanism and Properties. *Chem. Mater.* **2004**, *16*, 4896–4904.
- (63) Gupta, S. K.; Kadam, R. M.; Natarajan, V.; Godbole, S. V. Nanoparticles of $\text{Sr}_{0.995}\text{Gd}_{0.005}\text{ZrO}_3$ -gel-combustion synthesis, characterization, fluorescence and EPR spectroscopy. *Mater. Sci. Eng., B* **2014**, *183*, 6–11.
- (64) Rasouli, S.; Moeen, S. J. Combustion synthesis of Co-doped zinc oxide nanoparticles using mixture of citric acid–glycine fuels. *J. Alloys Compd.* **2011**, *509*, 1915–1919.
- (65) Huang, Y.; Cheng, X.; Li, Y.; Shi, D.; Li, G.; Xu, K. Effect of sol-gel combustion synthesis of nanoparticles on thermal properties of KNO_3 – NaNO_3 . *Sol. Energy Mater. Sol. Cells* **2018**, *188*, 190–201.